Advanced Libya-4 radiometric and atmospheric characterization utilizing moderate resolution imaging spectroradiometer and visible infrared imaging radiometer suite full-scan reflective solar band measurements

David R. Doelling,[a,*] Conor Haney,[b] Prathana Khakurel,[b] Rajendra Bhatt[b] [a] Benjamin Scarino,[a] and Arun Gopalan[b]

[a]NASA Langley Research Center, Hampton, Virginia, United States
[b]Analytical Mechanics Associates, Hampton, Virginia, United States

ABSTRACT. The NASA Clouds and the Earth's Radiant Energy System (CERES) project provides observed flux and cloud products to the climate science community. The CERES instruments, along with the moderate resolution imaging spectroradiometer (MODIS) and visible infrared imaging radiometer suite (VIIRS) imagers, are onboard the Terra, Aqua, NPP, and NOAA20 satellites. To produce seamless multi-platform integrated products, long-term sensor stability and inter-calibration are required. Inter-calibration between sensors within the same Sun-synchronous orbit relies on Earth invariant targets because simultaneous nadir overpasses are not possible. To facilitate inter-calibration efforts, the CERES Imager and Geostationary Calibration Group has improved the Libya-4 target characterization. Improvements include full scan angle characterization to enable daily observations, clear-sky identification using individual scan angle dynamic spatial homogeneity thresholds, and atmospheric corrections. The water vapor correction was found to be effective across the full scan, whereas the ozone and aerosol corrections were less effective. The atmospheric-corrected normalized radiance temporal fluctuations are similar across scan angles and spectral bands and between the MODIS and VIIRS imagers, suggesting that the fluctuations are a result of the natural variability of the Libya-4 surface reflectance. The Libya-4 surface variability is more than likely caused by changes in the prevailing winds that alter sand dune orientation and resulting shadows. The full-scan-imager atmosphere and angle corrected reflected solar band radiance trend standard errors are between 0.6% and 1.0%, and for near-nadir observations, they are between 0.5% and 0.8%. The advanced characterization suggests that the Libya-4 short-term surface reflectance anomalies may need to be considered for imager stability monitoring and inter-calibration efforts.

---

*Address all correspondence to David R. Doelling, david.r.doelling@nasa.gov

1 Introduction

The NASA Clouds and the Earth's Radiant Energy System (CERES)[1] energy balanced and filled product provides the scientific community with observed TOA shortwave (SW) and longwave broadband fluxes for climate monitoring and climate model validation.[2] CERES instruments are flying on the Terra, Aqua, NPP, and NOAA20 low Earth orbit Sun-synchronous satellites. The CERES-measured radiances need to be converted to fluxes using angular directional models,[3] which are based on the cloud properties retrieved from the accompanying moderate resolution imaging spectroradiometer (MODIS) and visible infrared imaging radiometer suite (VIIRS) imagers.[4–6] The CERES synoptic 1 deg spatially gridded (SYN1deg) product relies on five contiguous, concurrent geostationary satellite (GEO) imagers to infer the regional diurnal flux between the CERES measurements.[7] Consistent MODIS, VIIRS, and GEO cloud properties and imager radiances are necessary to process multi-satellite, climate-quality flux products. To achieve consistency in both cloud retrieval and in GEO-derived narrowband-to-broadband flux across multiple imagers, the analogous imager channel radiances are radiometrically scaled to a common calibration reference.

The Aqua, NPP, and NOAA20 satellites are in the same mean 1:30 PM local equator crossing time (LECT) orbit, and all satellites have 16-day orbit repeat cycles. Because Aqua has the lower altitude (705 km) compared with either NPP or NOAA20 (830 km), the Aqua ground track intersects NPP or NOAA20 every 64 h. For the CERES Edition 4 products, the NPP-VIIRS and NOAA20-VIIRS reflective solar band (RSB) channel radiances were radiometrically scaled to the Aqua-MODIS Collection 6.1 (C6.1) calibration reference utilizing all-sky tropical ocean ray-matched (ATO-RM) MODIS and VIIRS coincident radiance pairs.[8] The CERES project validated the ATO-RM MODIS and VIIRS radiometric scaling factors with the inter-calibration factors derived from the Libya-4, Dome-C, and deep convective cloud (DCC) invariant Earth targets, as well as using GEOs as transfer radiometers. Beginning in 2022, the Aqua and Terra (10:30 AM LECT) satellites slowly started drifting toward the terminator and will be decommissioned after 2026 when their projected LECT exceeds 3:00 PM and 9:00 AM, respectively. The frequency of coincident MODIS and VIIRS ATO-RM radiance pairs rapidly decrease as the orbital drift advances.

The NPP and NOAA20 spacecraft are located a half an orbit apart in the same orbit prior to 2024, wherein the NPP ground track is 8 days ahead of the NOAA20 ground track.[9] Having two sensors at half an orbit apart facilitates uninterrupted operations in case of sensor failure and provides a maximum daily observed time separation of ~45 min between sensors. Pseudo-invariant calibration site (PICS) inter-calibration allows all sensors in the same orbit to be radiometrically scaled without time matched observations. The PICS inter-calibration uncertainty is tied to the temporal variability of the PICS surface reflectance, surface bidirectional reflectance distribution function (BRDF), gaseous absorption, and scattering within the atmospheric column. A well-characterized PICS is well suited for monitoring sensor temporal stability. For example, PICS were characterized by scanning or viewing angle to resolve the MODIS on-orbit scan angle dependency caused by uneven temporal degradation of the ageing scan angle mirror.[10,11]

The CERES Imager and Geostationary Calibration Group (IGCG) continues to make incremental advances characterizing the Libya-4 PICS. The goal is to facilitate the inter-calibration of the Aqua-MODIS and successive VIIRS sensors to place them all on the same radiometric scale, thereby ensuring consistent CERES cloud and flux retrievals across the instrument records. An additional goal of the Libya-4 characterization is to provide an independent assessment of the MODIS and VIIRS L1b RSB stability and scan angle response. The Libya-4 characterization may have the added benefit of enabling the monitoring of the CERES broadband SW channel stability.

1.1 Background

Following the recommendation of the Committee on Earth Observation Satellites (CEOS) Working Group on Calibration and Validation (WGCV), the Libya-4 PICS, which is one of the driest, least cloudy, and highly reflective desert PICS,[12] has been used extensively for post-launch radiometer drift monitoring and sensor pair radiometric scaling of high, medium, and low-resolution satellite imagers, including Landsat, Sentinel-MSI/OLCI/SLSTR, AVHRR, ATSR,

MERSI, MODIS, VIIRS, DSCOVR-EPIC, and Meteosat GEO imagers. Libya-4 is located in an extensive sand dune region nearly void of vegetation, positioned near the northeast Libya and Egypt border, with an elevation of 118 m and monthly mean precipitation of ∼1 mm. Staylor[13] discovered the potential of the nearby Saharan desert PICS (17°N to 27°N and 3°W to 27°E) for monitoring the CERES precursor, Earth radiation budget experiment (ERBE) broadband SW channel calibration stability. Later, Staylor[14] was able to determine the degradation of the AVHRR sensors utilizing the Libyan desert (20°N to 30°N and 20°E to 30°E) based on the ERBE calibration approach. Rao et al.[15] utilized the Libyan desert (21° to 23°N and 28°E to 29°E) to monitor the degradation of the NOAA-7, 9, and 11 AVHRR sensors. Cosnefroy et al.[16] established the Saharan and Arabian PICS locations, nomenclature, and initial stability assessment, including the Libya-4 site (28.55°N and 23.39°E), that were suitable for assessing the visible sensor calibration over multiple solar and viewing conditions. Over the years, follow-on studies have confirmed that Libya-4 is indeed one of the most stable and spatially uniform PICS suitable for sensor stability validation.[17–19] Due to the stability of the Libya-4 PICS, it was utilized to tie the 40-year AVHRR record to the Aqua-MODIS[20–22] and SeaWiFS[23] calibration references.

Once the temporal stability of Libya-4 was established, the observed viewing and solar angular dependencies of the surface BRDF were characterized. The Libya-4 sand dunes have an average height of 60 m and tend to reflect more in the backscatter than in the forward scatter direction, especially for large solar angles.[24] Bacour et al.[19] stated that the Libya-4 multi-angle PARASOL observations reveal a surface anisotropy of less than 10%. Wu et al.[25] found that the Libya-4 BRDF is nearly Lambertian for viewing zenith angles (VZA) less than 25 deg and for solar zenith angles (SZA) less than 50 deg by comparing Lambertian and semi-empirical BRDF models. Bhatt et al.[26] examined Meteosat-9 imager daily clear-sky TOA radiances under off-nadir (VZA of ∼42 deg) viewing conditions over Libya-4 and reported that the average daily inter-annual variability for visible wavelengths was below 1%. Given the Libya-4 minimal inter-annual variability, the CERES IGCG radiometrically scaled successive Meteosat geostationary imagers operating at 0 deg longitude to a common calibration reference.[27] Chang et al.[28] found that the Terra and Aqua MODIS derived semi-empirical and empirical BRDF models were similar. Mishra et al.[29] derived a Terra-MODIS TOA reflectance model with respect to SZA and remarked that higher order Ross–Li kernel functions were no better than the simple linear model for near nadir measurements.

Because the BRDF effects are small over desert sites, many desert calibration studies have simply correlated sensor reflectances with SZA. Wu and Zhong[30] utilized Chinese desert sites and linearly regressed the AVHRR reflectance with cosine SZA to determine the AVHRR degradation. Heidinger et al.[20] found a second order relationship between AVHRR TOA reflectance and SZA over Libya-4. Wu et al.[31] derived a second order cosine SZA relationship with TOA reflectance over Libya-4 and found that the observed Terra and Aqua-MODIS 0.64-μm BRDF corrected reflectance record had a trend standard error of 1.0% and 0.9%, respectively. Initially, the CERES IGCG simply regressed near-nadir observed TOA radiances by cosine SZA (CSZA), but separately for forward and backscatter conditions, because the azimuthally dependent radiances diverged especially for shorter wavelengths.[32–34] More recently, the CERES IGCG began binning the near-nadir observations by repeat day or by scan angle.[35,36]

Although the Libya-4 atmospheric column is extremely dry, water vapor absorption impacts many of the near infrared (NIR) and short-wave infrared (SWIR) band TOA radiances, especially during the summer when hot temperatures allow for greater water vapor burden even for very low relative humidity conditions.[20,28] The Libya-1 and Libya-4 PICS have the least seasonal precipitable water (PW) and ozone (O3) variation of all Saharan desert PICS (Bacour et al.[19] see their Fig. 10). Yu and Wu[37] noted that the 11-μm minus 12-μm brightness temperature difference was correlated with PW as well as the AVHRR 0.86-μm band TOA reflectance. The PW-corrected AVHRR 0.86-μm band reflectance uncertainty was reduced from ∼3% to 1.7%. Multiple studies utilize Hyperion spectra to account for atmospheric absorption and spectral response function differences dependent on viewing and solar angles.[29,38–41] Other studies employed atmospheric correction to account for the ozone and water vapor absorption as well as aerosol scattering over

Libya-4[42–45] and Dunhuang[46] deserts. The CERES IGCG has recently correlated the RSB water vapor absorption with multiple PW sources.[35,36]

1.2 Outline

This work is a continuation of the previous Libya-4 characterization studies of Doelling et al.[35] performed to facilitate the CERES IGCG objectives of MODIS and VIIRS imager stability assessment and radiometric scaling. The Terra/Aqua MODIS and NPP/NOAA20 VIIRS reflective solar bands (RSB) are characterized across all angular conditions observed during the 16-day repeat cycle. The previous work characterized only near nadir measurements having view angles less than 30 deg. The utilization of the full scan offers daily observations over the site, thereby greatly increasing the sampling and allowing for a more rigorous identification of pristine clear-sky events. The clear-sky identification is based on the application of both broad and dynamic angular dependent spatial homogeneity thresholds, applied to both the 0.65-μm and 1.61-μm channels, which are the channels least impacted by the atmospheric column. The previous study simply utilized a 0.65-μm channel broad spatial homogeneity threshold to determine clear-sky conditions. This study applies the same characterization across the MODIS and VIIRS imagers, whereas the previous study simply focused on Aqua-MODIS.

Each angular bin, defined by viewing angle and by forward or backscatter azimuth conditions, is characterized by a second order cosine solar zenith relationship, with inclusion of linear PW, O3, and aerosol optical depth (AOD) atmosphere correction terms. This study greatly reduced the number of terms required for characterization compared with the previous effort and thereby mitigates the risk of overfitting. This study also linearly correlated several PW, O3, and AOD daily measurement datasets with the observed TOA channel radiance to find the datasets providing the most effective atmospheric corrections. The atmospheric correction is further validated by the consistency of the relative reflectance trending across RSB and scan angle. Figure 1 provides a flowchart of both the overall methodology and clear-sky identification. The MODIS and VIIRS analogous channel Libya-4 normalized reflectance temporal trends are also compared. Finally, a table of MODIS and VIIRS RSB trend standard errors, with and without atmospheric correction, are provided for full scan and near nadir observations. Section 2 describes the Libya-4 methodology, and Sec. 3 gives the validation results. Concluding remarks and future research are discussed in Sec. 4.
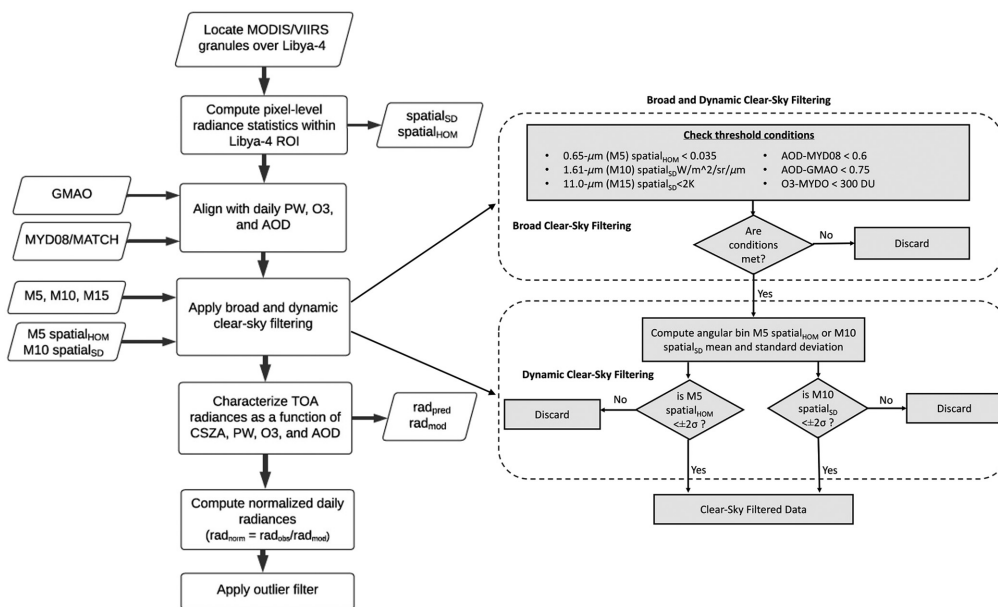
Fig. 1 Schematic of the methodology described in Sec. 2 and the clear-sky identification denoted in Sec. 2.3.

Table 1 MODIS and VIIRS RSB nomenclature as a function of wavelength.

μm	0.48	0.55	0.65	0.86	0.91	1.24	1.61	2.1	2.2
MODIS	B3	B4	B1	B2	B17	B5	B6	B7	—
VIIRS-M	M3	M4	M5	M7	—	M8	M10	—	M11
VIIRS-I	—	—	I1	—	—	—	I3	—	—

2 Methodology

2.1 Data

The Terra-MODIS, Aqua-MODIS, NPP-VIIRS, and NOAA20-VIIRS data used in this study are a reformatted subset of the original NASA MODIS C6.1 L1b product and the NASA VIIRS Land Science Investigator-led Processing System (Land SIPS) L1b Collection 2. In support of CERES, these data are generated at the Atmospheric Science Data Center Distributed Active Archive Center (ASDC DAAC) located at the NASA Langley Research Center. The MODIS C6.1 radiances were converted to C7 using LUTs provided by the MODIS characterization support team (MCST) and are a function of scan angle, mirror side, and day. The differences between C7 and C6.1 calibrations are outlined in previous studies.[47] The CERES project subsamples the MODIS 1-km and VIIRS L1B 750-m pixels by utilizing every alternate line and pixel. Table 1 describes the MODIS and VIIRS channel naming convention referred to in the text.

This study compares several sources of PW, O3, and AOD measurements utilized in the Libya-4 PICS atmospheric correction strategy. The CERES project utilizes the Goddard Space Flight Center (GSFC) Global Modeling and Assimilation Office (GMAO) Goddard Earth Observing System 5.4.1 reanalysis product to describe the regional hourly atmospheric profile.[48] The GMAO PW (PW-GMAO) is based on the assimilation of Aqua-atmospheric infrared sounder and the advanced microwave sounding unit-A observations, as well as ground-based soundings. The GMAO ozone (O3-GMAO) is derived from NPP and NOAA20 - ozone mapping and profiler suite and Aura-ozone monitoring instrument UV observations. The GMAO assimilations strive for a consistent 40-year reanalysis dataset incorporating overlapping satellite records.

The daily Aqua-MODIS MYD08-D3 product provides PW, ozone, and AOD retrievals. The MYD08-D3 NIR approach (PW-RSB) compares the 0.905, 0.936, and 0.94-μm water vapor absorbing channels with the 0.865 and 1.24-μm atmospheric window channels.[49,50] The MYD08-D3 IR (PW-IR) approach mainly relates the 6.72 and 7.33-μm water vapor channels with the 8.55-μm window channel.[51] The MYD08-D3 ozone (O3-MYD08) is retrieved from the MODIS 9.6-μm channel.[51] The NASA-GSFC Aqua-MODIS MYD04_L2 product combines the dark target[52] and deep blue[53] AOD obtained during clear-sky events (AOD-MYD08). Over Libya-4, the MODIS deep blue algorithm is employed. The multi-scale atmospheric transport and chemistry (MATCH) Eulerian three-dimensional model assimilates MODIS AOD retrievals and advects the aerosols in 3-hourly time-steps (AOD-MATCH).[54] The desert dust-sizes are determined by wind speed. The AOD-MATCH, PW-GMAO, and O3-GMAO measurements are obtained from the CERES SYN1deg product[55] whereas the PW-RSB, PW-IR, O3-MYD08, and AOD-MYD08 are obtained from the MYD08-D3 product[56] measurements.

A comparison of the PW measurements over Libya-4 is shown in Fig. 2. The daily PW-GMAO and PW-RSB clear-sky identified (see Sec. 2.3) observations are linearly correlated, revealing that the PW-RSB values are increasing at a greater rate than the PW-IR values [Fig. 2(a)]. PW-GMAO seems to have a nonlinear relationship and overall lower values than the PW-RSB values [Fig. 2(b)], but higher values than those of PW-IR [Fig. 2(c)]. The PW dataset that provides the greatest correlation with the daily observed clear-sky identified TOA radiances is discussed in Sec. 2.5.

2.2 Libya-4 Angular Bins

The CERES IGCG Libya-4 PICS methodology follows Bhatt et al.[33] and Doelling et al.[35] The instantaneous Libya-4 MODIS and VIIRS pixel radiances are averaged over the 1 deg × 1 deg
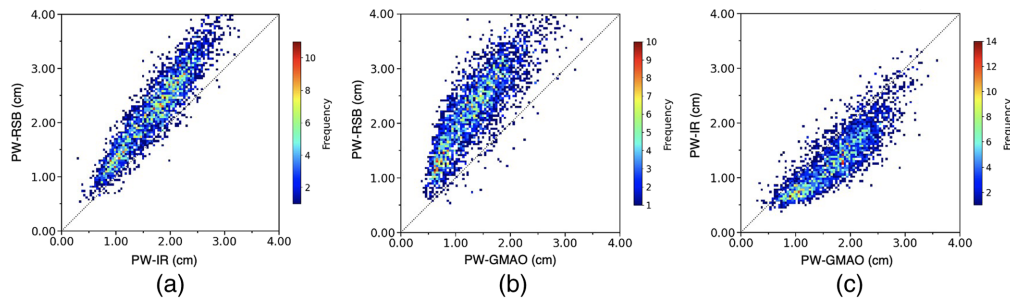
Fig. 2 Comparison of the Libya-4 daily (a) PW-RSB and PW-IR, (b) PW-RSB and PW-GMAO, and (c) PW-IR and PW-GMAO clear-sky identified observations over the NPP record.
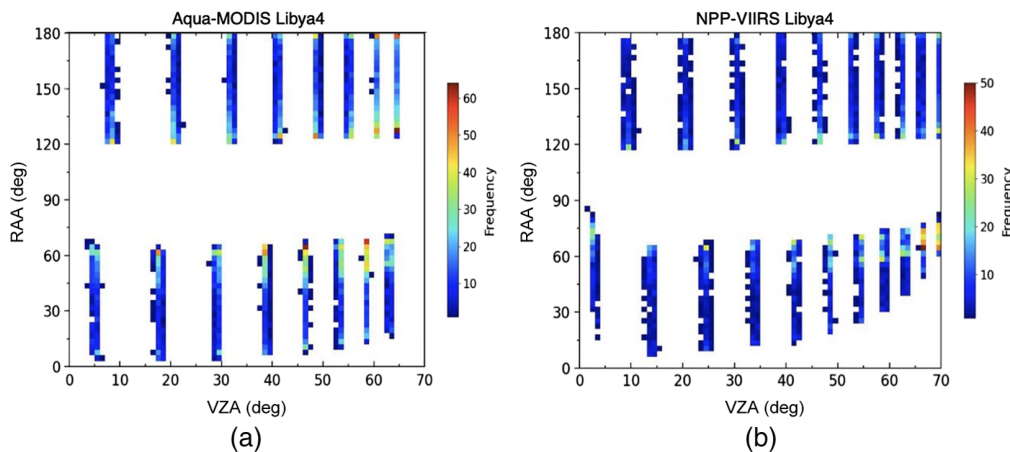
Fig. 3 Libya-4 (a) Aqua-MODIS and (b) NPP-VIIRS VZA and RAA, with RAA of 0 deg representing forward scatter, observed frequency distributions. The MODIS and VIIRS observations are stratified into 16 and 21 angular bins, respectively.

region of interest (ROI) centered at 28.6°N latitude and 23.4°E longitude. If the L1b granule boundaries intersect the ROI, the two granules are first concatenated to ensure complete spatial sampling across the entire ROI. The instantaneous observations are easily stratified into angular bins by view zenith angle (VZA) and relative azimuth angle (RAA), as shown in Fig. 3. See also Fig. 1 in Chang et al.[28] The Terra and Aqua orbit altitude of 720-km limits the MODIS Earth view scan angle to 65 deg [Fig. 3(a)]. There are eight backscatter VZA and eight forward scatter VZA bins, with each bin representing one repeat cycle day. Due to the higher 833-km altitude of the NPP and NOAA20 satellites, the VIIRS swath encompasses a scan angle of 70 deg and provides 21 angular bins, 16 for each repeat cycle day and 5 from neighboring orbits where the swaths overlap Libya-4.

2.3 Libya-4 Clear-Sky Identification

The key to successful clear-sky identification over Libya-4 is finding RSBs that are the least susceptible to gaseous absorption and aerosol scattering over the Libya-4 target, especially when observing oblique angular bins. The 0.86, 1.24, and 2.15-μm channels are impacted by water vapor absorption, whereas the 0.48 and 0.55-μm channels are impacted by aerosols and ozone absorption, respectively. This leaves the 0.65 and 1.6-μm channels to determine clear-sky conditions. This study relies on spatial homogeneity filters as an effective way to identify clear-sky events.[57] Clear-sky events are more spatially uniform than cloudy events. Also, the spatial clear-sky uniformity is assumed to remain consistent over time. The clear-sky events in Fig. 4 are revealed by the densely clustered daily homogeneity values, whereas the cloudy events have a wide range of homogeneity values, which exceed the clear-sky values. Two spatial homogeneity filters are evaluated: the pixel radiance standard deviation over the ROI (spatial$_{SD}$) and a spatial homogeneity factor computed by dividing the spatial$_{SD}$ by the mean radiance
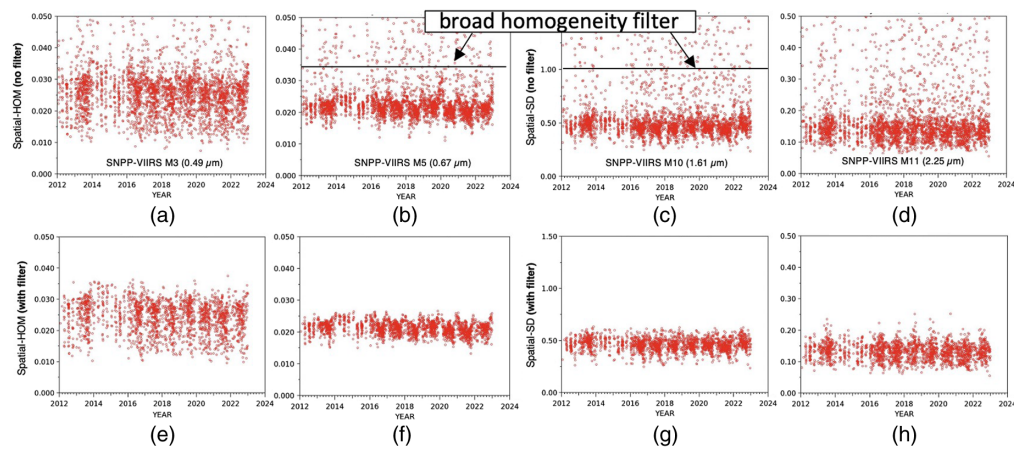
Fig. 4 Libya-4 NPP-VIIRS daily observed (a) M3 spatial$_{HOM}$, (b) M5 spatial$_{HOM}$, (c) M10 spatial$_{SD}$, and (d) M11 spatial$_{SD}$. Panels (e)–(h) same as panels (a)–(d), except after application of the broad and dynamic clear-sky filters. The clear-sky spatial homogeneity values are much lower and similar (densely packed) in time than the cloudy events. The broad homogeneity filter threshold is overlaid in panels (b) and (c).

(spatial$_{HOM}$). It was found for channels with wavelengths less than 1 μm that the spatial$_{SD}$ has a distinct seasonal fluctuation, with greater values in winter and smaller values in summer. A simple spatial$_{SD}$ threshold determined for winter conditions would not filter out all cloudy events during the summer. For visible wavelengths (<1 μm), the spatial$_{HOM}$ was applied. However, the spatial$_{SD}$ for wavelengths greater than 1 μm had a reduced seasonal oscillation, and for these wavelengths, a spatial$_{SD}$ filter was applied.

The Libya-4 clear-sky filtering relies on a two-step approach that consists of broad and dynamic clear-sky filtering. The following broad clear-sky thresholds are utilized; 0.65-μm (VIIRS M5) spatial$_{HOM}$ < 0.035, 1.61-μm (VIIRS M10) spatial$_{SD}$ < 1.0 Wm^{-2} sr^{-1} μm^{-1}, 11.0-μm (VIIRS M15) spatial$_{SD}$ < 2 K, AOD-MYD08 <0.6, AOD-GMAO <0.75, and O3-MYDO <300 DU. The IR spatial$_{SD}$ was more effective than the visible spatial$_{SD}$ at detecting high thin cirrus and their associated shadows. The AOD and O3 parameter thresholds were necessary for removing retrieval outliers, which otherwise may impact the subsequent atmospheric corrections. Figures 4(b) and 4(c) reveal the NPP-VIIRS daily M5 spatial$_{HOM}$ and M10 spatial$_{SD}$ observations overlaid by their associated homogeneity thresholds. Note that the NPP-VIIRS M3 (0.49-μm) channel has a much larger clear-sky spatial$_{HOM}$ range [Fig. 4(a)] than that of the M5 channel [Fig. 4(b)] because it is impacted by both aerosols and Rayleigh scattering. The M3 channel has increased Rayleigh scattering and darker surface reflectance than the M5 channel. Similarly, the M11 channel has a broader clear-sky standard deviation range [Fig. 4(d)] than the M10 channel [Fig. 4(c)] because it is impacted by WV absorption. Overall, the broad clear-sky filters remove ~40% of the observations.

To remove any remaining cloudy events, a dynamic clear-sky filter is applied individually to each angular bin. The angular bin M5 spatial$_{HOM}$ or M10 spatial$_{SD}$ mean and standard deviation are computed, after which any observations that exceed twice the standard deviation from the mean are removed. The dynamic filtering process resulted in the removal of an additional 9% of the total observations, predominantly eliminating the winter M5 spatial$_{HOM}$ spikes [compare Fig. 4(b) with Fig. 4(f) during 2020]. The 0.65 and 1.61-μm dynamic filtering effectively removed most of the daily spatial$_{HOM}$ outliers across all RSB channels (see Fig. 4, second row). The few remaining M3, M4, M5, and M10 outliers (1.7% of total) are removed utilizing a normalized radiance outlier (3σ) filter, leaving 49% of the daily observations for stability monitoring.

2.4 Libya-4 Angular Radiance Models

The MODIS and VIIRS L1b radiances were converted to 1-AU by accounting for the Earth-Sun distance. For each MODIS and VIIRS angular bin, the Libya-4 observed radiances are characterized by applying a second order fit with respect to CSZA utilizing Eq. (1) to obtain the
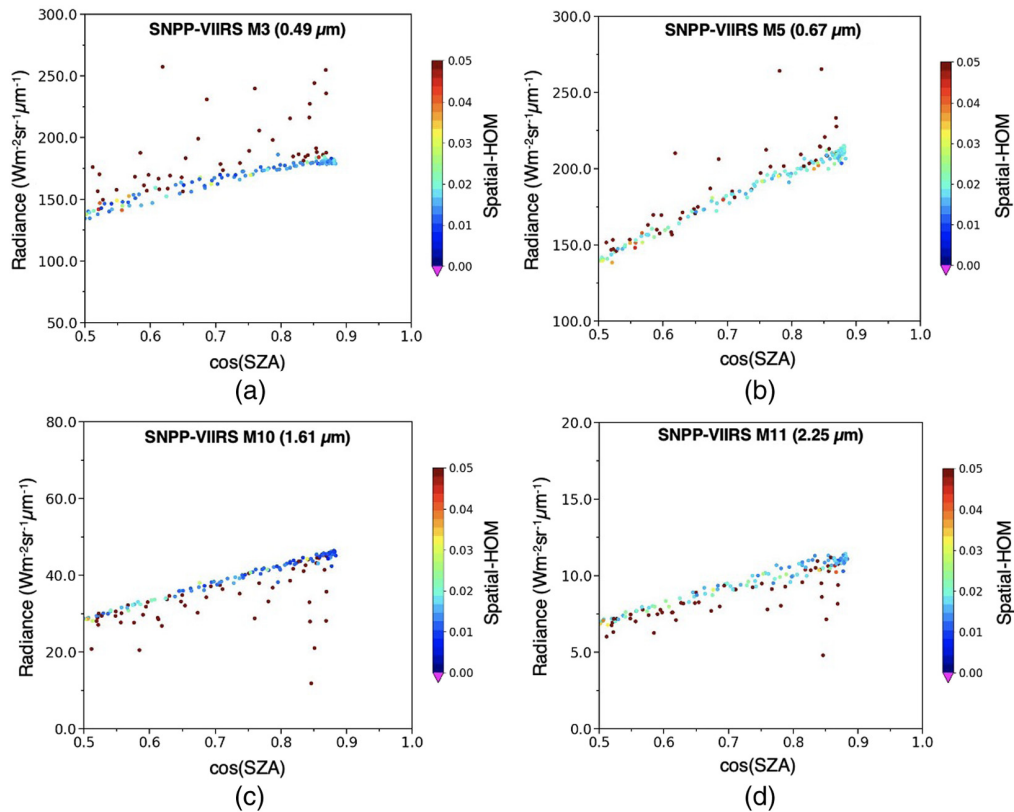
Fig. 5 Libya-4 NPP-VIIRS daily all-sky (not clear-sky filtered) observed (a) M3, (b) M5, (c) M10, and (d) M11 radiances (Wm^{-2} sr^{-1} μm^{-1}) as a function of cos(SZA) for the 68 deg < VZA < 70 deg and 90 deg < RAA < 180 deg backscatter angular bin. The daily radiances are color coded by the spatial$_{HOM}$ factor. Note that, for all bands, the cloudy erratic radiances (dark brown points) are easily identified by their large spatial$_{HOM}$, leaving the clear-sky radiances, which are well correlated.

TOA BRDF coefficients (g_0, g_1, and g_2) and thereby compute the predicted radiances (Rad$_{pred}$):

$$\text{Rad}_{pred} = g_0 + g_1 * \cos(\text{SZA}) + g_2 * \cos(\text{SZA})^2. \tag{1}$$

To demonstrate the efficacy of the spatial homogeneity filter for identifying pristine clear-sky conditions, all clear and cloudy Libya-4 daily radiance observations for the most oblique backscatter bin are plotted in Fig. 5 as a function of CSZA and are color coded by their spatial$_{HOM}$ values. For the M3 and M5 bands shown in Figs. 5(a) and 5(b), respectively, the brighter radiances are associated with greater spatial$_{HOM}$ (dark red points) than the darker clear-sky radiances, which are highly correlated with CSZA having smaller spatial$_{HOM}$ (blue points). For the M10 and M11 bands, the clouds are darker than the bright underlying desert. Figures 5(c) and 5(d) show that cloudy M10 and M11 radiances are darker and have larger spatial$_{HOM}$ (dark red points) than the brighter clear-sky radiances, which have a smaller spatial$_{HOM}$ (blue points). The second order regression standard error [Eq. (1)] for all observations for this angular bin is shown in Table 2 under the no filter row. The broad filter thresholds (Sec. 2.3) remove most of the cloudy events. The M5 and M10 channel clear-sky dynamic filter reduces the fit standard error below 1%. If the large spatial$_{HOM}$ events were not related with cloudy events, then the spatial$_{HOM}$ filtering would not reduce the radiance fit standard error. The success of spatial homogeneity filters avoids utilizing RSB reflectance thresholds, which would otherwise be influenced by wavelength-dependent cloud brightness.

The Libya-4 NPP-VIIRS M3, M5, and M11 individual angular bin [Eq. (1)] models are shown in Fig. 6. The M3 angular bin models reveal that the Libya-4 radiance is dependent

Table 2 Libya-4 NPP-VIIRS Eq. (1) regression standard error in % for the 68 deg < VZA < 70 deg and 90 deg < RAA < 180 deg backscatter angular bin shown in Fig. 3. The no filter regression corresponds to the Fig. 5 plots, which utilizes all daily (all-sky) observations. The broad filter applies the static spatial homogeneity thresholds, whereas clear sky includes both the static and dynamic spatial homogeneity thresholds. Note that, for non-absorbing bands (M5 and M10), the clear-sky fit standard error is less than 1%.

	M3	M5	M10	M11	Count
No filter	13.19	4.96	11.23	7.95	172
Broad filter	1.31	1.18	1.21	2.50	98
Clear sky	1.14	0.99	0.93	2.52	76

(a) (b) (c)
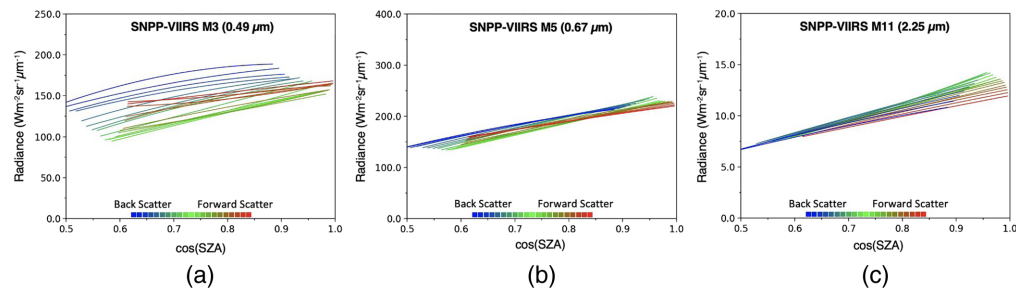
Fig. 6 Libya-4 NPP-VIIRS daily predicted (a) M3, (b) M5, (c) M11, radiance $(Wm^{-2} sr^{-1} \mu m^{-1})$ as a function of CSZA for the 21 angular bins color coded by scan angle; the blue bins are in the backscatter direction or the left side of the scan, the red bins are in the forward scatter direction or right side of the scan, and nadir scans are shown in green.

on the azimuth and view angle. The M5 shows very similar angular bin models and is the most Lambertian channel. M11 shows similar radiances for small CSZA and diverges significantly for near overhead Sun conditions. The RSB angular bin models that are not shown gradually transition by wavelength between Fig. 6 angular models. It may be possible to group the near nadir angular bin radiances into a singular angular bin model [Eq. (1)]; however, by including large view angle bins, the radiances cannot be resolved with a singular angular bin model. The Roujean semi-empirical model[58] was compared with the second order CSZA model. For near nadir and large VZA bins, the trend standard errors were comparable; however, for the midrange VZA bins, the Roujean trend standard errors were twice as large as the CSZA model (not shown). The second order CSZA relationship describes the observed clear-sky radiances with the fewest terms.

2.5 Libya-4 Atmospheric Correction

In this section, we correlate the PW, O3, and AOD retrievals with the TOA observed clear-sky radiances as a function of wavelength. The Libya-4 TOA radiances are modeled by applying a second order fit to the observed radiances with respect to CSZA, similar to Eq. (1), and incorporating the linear coefficient terms for PW, O3, and AOD, as illustrated in Eq. (2). Equation (2) coefficients are computed for each of the 16 MODIS and 21 VIIRS angular bins as

$$\mathrm{Rad_{mod}} = a_0 + a_1 * \cos(\mathrm{SZA}) + a_2 * \cos(\mathrm{SZA})^2 + a_3 * \mathrm{PW} + a_4 * \mathrm{O3} + a_5 * \mathrm{AOD}. \quad (2)$$

The normalized radiances $(\mathrm{rad_{norm}})$ are computed by dividing daily observed clear-sky radiances $(\mathrm{rad_{obs}})$ by the predicted or modeled radiance $(\mathrm{rad_{mod}})$ from Eq. (2), as

$$\mathrm{rad_{norm}} = \mathrm{rad_{obs}}/\mathrm{rad_{mod}}. \quad (3)$$

The linear regression standard error $(\mathrm{trend_{SE}})$ is computed from the clear-sky daily $\mathrm{rad_{norm}}$ observations across all angular bins over the record. To determine the atmospheric correction

Table 3 Libya-4 NPP-VIIRS Eq. (2) regression standard error in % across all angular bins as a function of a single atmospheric dataset (see Sec. 2.1). The CSZA-only represents the Eq. (1) linear regression standard error (trend$_{SE}$) in % of the clear-sky daily rad$_{norm}$ observations. The bold text denotes the trend$_{SE}$ reduction in % by adding a single atmospheric correction term in Eq. (2) compared with the CSZA-only trend$_{SE}$. For comparison, M5 and M10 bands, which are the least sensitive to the atmospheric column, have a CSZA-only trend$_{SE}$ of 0.686% and 0.636%, respectively.

Band	CSZA-only	AOD MYDO08	AOD MATCH	O3 GMAO	O3 MYDO8	PW RSB	PW IR	PW GMAO
M3	1.102	1.042 **5.8%**	1.058 **4.0%**	—	—	—	—	—
M4	0.885	—	—	0.846 **4.4%**	0.860 **2.9%**	—	—	—
M7	0.745	—	—	—	—	0.630 **15.4%**	0.652 **12.5%**	0.658 **11.7%**
M8	1.051	—	—	—	—	0.627 **40.3%**	0.742 **29.4%**	0.722 **31.3%**
M11	1.923	—	—	—	—	0.733 **61.9%**	1.217 **36.7%**	1.022 **46.9%**

impact, Eq. (2) coefficients are computed for a single atmospheric parameter at a time, and the resulting trend$_{SE}$ is compared with the trend$_{SE}$ without utilizing atmospheric terms [Eq. (1)]. A comparison of the 3 PW sources of the trend$_{SE}$ in Table 3 shows that the PW-RSB has the lowest trend$_{SE}$ for the M7 (0.86 μm), M8 (1.24 μm), and M11 (2.25 μm) water vapor absorption channels. This is not surprising as the RSB channels were used to retrieve the water vapor in the PW-SRB dataset. Note that the M7 and M8 PW-RSB trend$_{SE}$ was very close to the M10 trend$_{SE}$, which was least impacted by the atmospheric column and indicates that the PW-RSB dataset was nearly optimal in estimating the radiance impact of PW.

The O3-GMAO UV based ozone retrieval is slightly more effective in predicting the M4 ozone absorption impact than the O3-MYD08 9.6-μm ozone retrieval. The ozone impact was minimal due to the small seasonal ozone fluctuations over Libya-4. The AOD-MYD08 is slightly more effective in determining the AOD impact on the M3 (0.49 μm) radiance because the AOD-MYD08 aerosols were directly retrieved during clear-sky events. Note that the AOD and O3 atmospheric corrections were minimal compared with the PW atmospheric correction reduction. Finding a more robust ozone and aerosol retrieval product or utilizing nonlinear terms with TOA reflectance is left for future studies. Similar results were obtained for NOAA20-VIIRS, Terra-MODIS, and Aqua-MODIS. There is no advantage in using the Terra-based PW-RSB, PW-IR, or AOD over their Aqua counterparts.

Based on the analysis in Table 3, the PW-RSB, O3-GMAO, and AOD-MYD08 datasets were used to determine the PW, O3, and AOD terms in Eq. (2). Figure 7(a) shows the Libya-4 NPP VIIRS M11 clear-sky daily rad$_{norm}$ without applying the atmospheric correction terms, which reveals a large seasonal oscillation of $\pm$5%, with the positive rad$_{norm}$ values occurring in spring and the negative rad$_{norm}$ values occurring in fall. A slight downward trend is observed (0.1%/year). Figure 7(b) shows the clear-sky daily atmosphere-corrected rad$_{norm}$ observations. No discernable seasonal oscillation is perceived, and the downward trend is reduced by half. Figure 7(b) reveals that all daily angular bin rad$_{norm}$ are equally dispersed, indicating that the atmospheric corrections are effective across all angular bins. The atmospheric correction reduced the trend$_{SE}$ by ∼63%, which is almost entirely due to the PW contribution for this band. The downward trend is discussed in the following sections and is more than likely due to the Libya-4 surface natural variability.
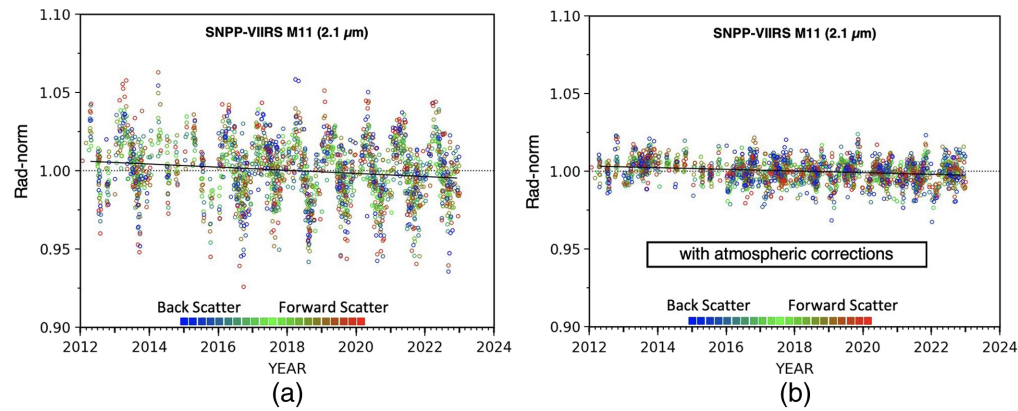
Fig. 7 Libya-4 NPP-VIIRS M11 clear-sky daily rad$_{norm}$ observations (a) CSZA-only terms [Eq. (1)] and (b) with atmospheric correction terms [Eq. (2)]. The daily rad$_{norm}$ observations are color coded by scan angle. The CSZA-only and with atmospheric correction trend$_{SE}$ are 1.92% and 0.71%, respectively, over the 11-year record. Similarly, the linear fit slopes are −0.011 and −0.0059, respectively.

3 Results

3.1 Libya-4 Scan Angle Consistency

The atmospheric correction is compared across angular bins. The atmospheric column radiance contribution is a function of the gaseous absorption contained within the channel spectral response and the combined SZA and VZA pathlength. If the atmospheric correction were perfect, the rad$_{norm}$ temporal variability across the observed pathlengths or angular bins would be similar and would follow the Libya-4 surface reflectance natural variability given that surface reflectance is near Lambertian. The seasonal or interannual gaseous absorption or aerosol variability, after atmospheric correction, should not be manifested in the temporal record. To facilitate the angular bin consistency comparison of the observations in Fig. 7, a 365-day running mean is applied to smooth the individual angular bin daily rad$_{norm}$ observations and is shown in Fig. 8. Figures 7(a) and 7(b) daily rad$_{norm}$ observations plots can be compared with Figs. 8(c) and 8(f) plots, where the latter plots have the 365-day running mean applied. The atmosphere correction terms reduced the overall temporal variability. Also, Fig. 8 atmospheric corrected plots show in-synch angular
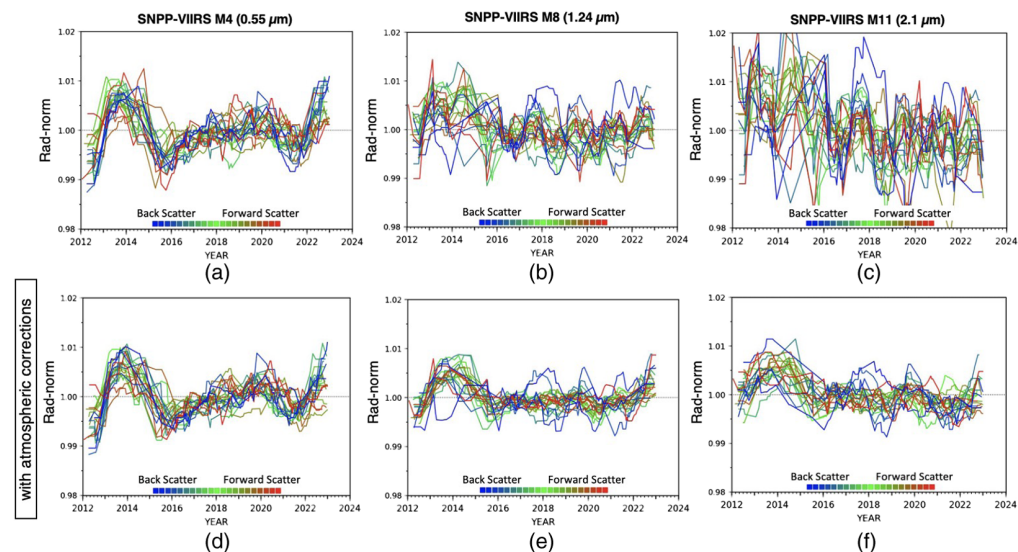
Fig. 8 Libya-4 NPP-VIIRS (a) M4, (b) M8, (c) M11, 365-day running mean rad$_{norm}$ observations using CSZA-only terms [Eq. (1)], color coded by angular bin. Panels (d)–(f) same as panels (a)–(c), except including atmospheric correction terms [Eq. (2)].
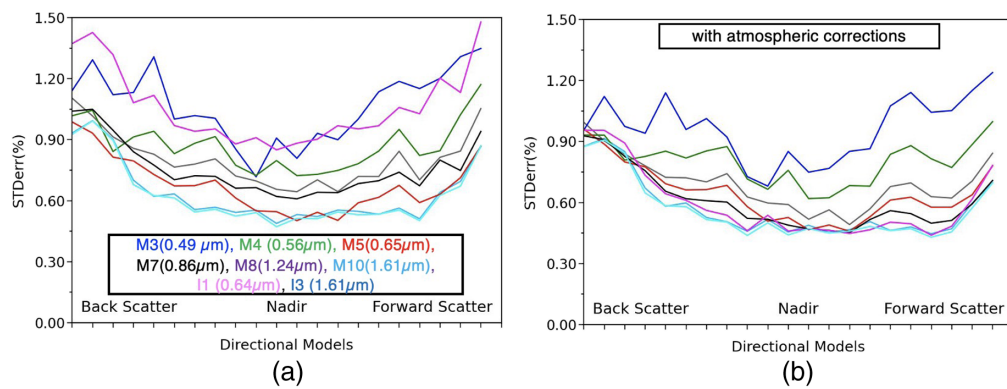
Fig. 9 Libya-4 NPP-VIIRS 365-day averaged spectral band trend$_{SE}$ using (a) CSZA-only terms [Eq. (1)] and (b) including atmospheric correction terms [Eq. (2)], color coded by spectral band as denoted by the legend. Note that many of the water vapor absorbing band angular bin trend$_{SE}$ are more similar to the M5 and M10 band trend$_{SE}$ after applying atmospheric correction terms.

bin temporal trending, especially for the 1.24 and 2.25-μm channels. The 0.55-μm ozone correction has tightened some of the noisier angular bin trends [compare Fig. 8(a) with Fig. 8(d)]. Also, the atmospheric-corrected 0.55-μm channel has similar temporal trending as the water vapor channels in Fig. 8.

If the atmospheric radiance contributions were perfectly removed, then the trend$_{SE}$ value should be similar across all RSBs for a given angular bin. Figure 9(a) shows the NPP-VIIRS RSB trend$_{SE}$ as a function of angular bin without atmospheric correction. The trend$_{SE}$ increases with increasing VZA, especially for backscatter conditions. As expected, the M5 and M10 have the lowest trend$_{SE}$ because these bands are the least impacted by atmosphere, whereas the bands impacted by water vapor and AOD have the highest trend$_{SE}$. Figure 9(b) shows the NPP-VIIRS band trend$_{SE}$ with atmospheric correction. The atmospheric correction reduced the M7, M8, and M11 trend$_{SE}$ and are more in line with the non-absorbing M5 and M10 channels. However, for the M3 and M4 channels, the trend$_{SE}$ was not significantly reduced with AOD and O3 atmospheric correction terms, suggesting that the AOD and O3 sources exhibited only minimal linear correlation with TOA radiance. The overall Libya-4 trend$_{SE}$ can be reduced by restricting the number of large VZA bins.

3.2 Libya-4 RSB Consistency

We now compare the atmospheric correction across the RSB. Without atmospheric corrections, the disparate channel gaseous absorption rad$_{norm}$ temporal fluctuations would be uncorrelated, if we assume that the Libya-4 surface reflectance temporal variability is minimally dependent on wavelength. Figure 10 left and right column plots display the MODIS and VIIRS RSB rad$_{norm}$ observations without and with atmospheric corrections, respectively. Note the large VIIRS M11 and MODIS B7 (yellow line) and B17 (gray line) water vapor absorption band rad$_{norm}$ temporal fluctuations. After atmospheric correction, the large fluctuations are greatly reduced and fluctuate in tandem with the other channels. Except for Terra-MODIS, the RSB rad$_{norm}$ fluctuations are very consistent, thereby validating that the RSB and angular-bin-specific atmospheric correction coefficients. The Terra-MODIS instrument onboard calibration system anomalies caused the spurious L1b radiance drifts. Furthermore, the Terra-MODIS solar diffuser door has remained in the open position since 2003, which increased the solar diffuser degradation for shorter wavelengths by 20% when compared with Aqua-MODIS. Finally, the 2016 Terra spacecraft anomaly increased the electronic cross-talk, especially for the SWIR bands.[59]

Note that the same positive $+0.5\%$ rad$_{norm}$ inflection during 2014 is present in the Terra-MODIS [Fig. 10(b)], Aqua-MODIS [Fig. 10(d)], and NPP-VIIRS [Fig. 10(f)] records. It seems that the RSB rad$_{norm}$ fluctuations are correlated across sensors. The 2014 rad$_{norm}$ spike also corresponds to the increased solar radiation exposure that degraded the MODIS and VIIRS solar diffusers.[60] However, the solar radiation exposure event should be accounted for in the L1B product by the onboard calibration system solar diffuser stability monitor.
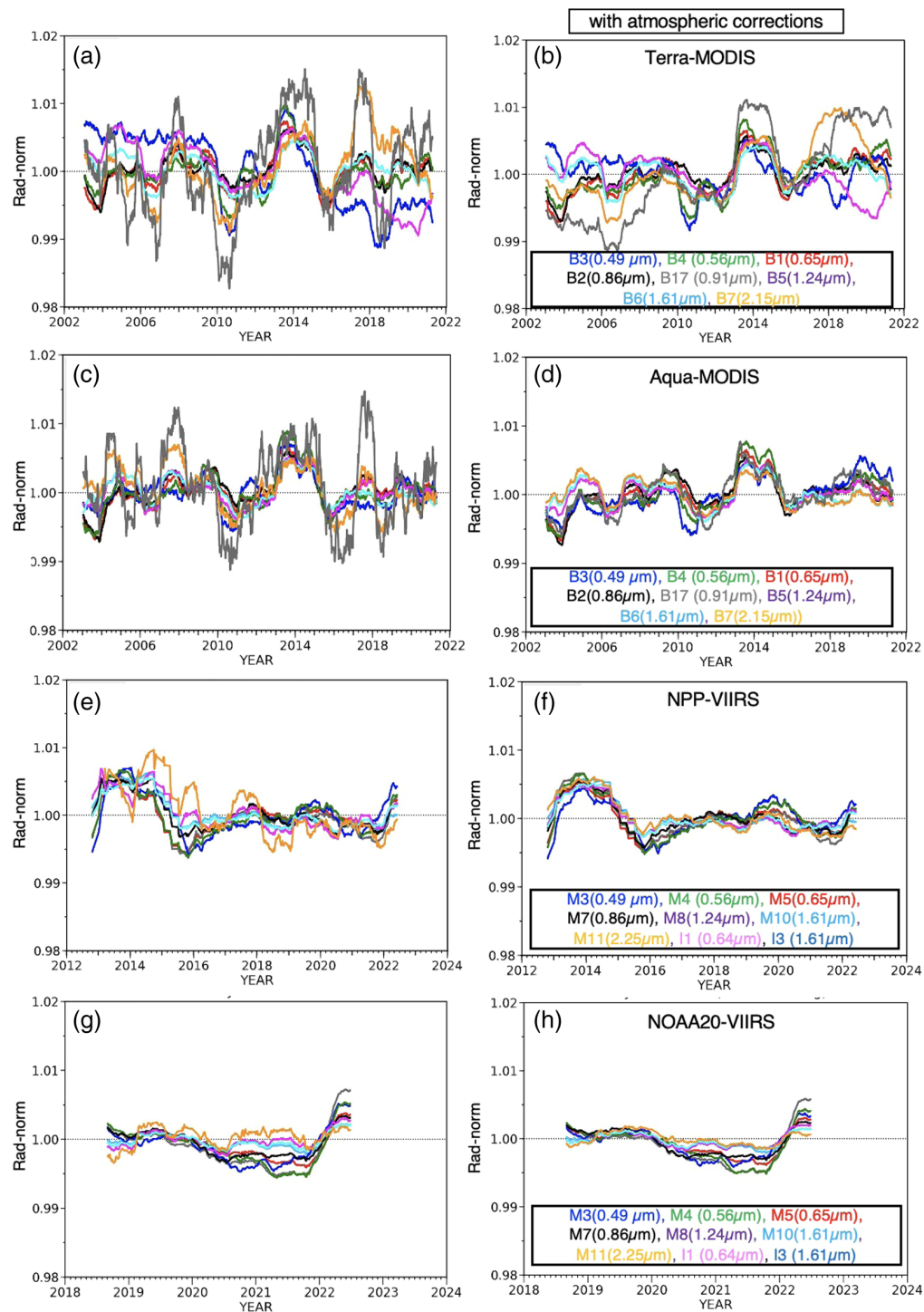
Fig. 10 Libya-4 Terra-MODIS 365-day averaged rad$_{norm}$ observations using (a) CSZA-only terms [Eq. (1)] and (b), including atmospheric correction terms [Eq. (2)], color coded by the spectral band according to the legend located in the right column plots. Panels (c) and (d) same as panels (a) and (b) except for Aqua-MODIS. Panels (e) and (f) same as panels (a) and (b) except for NPP-VIIRS. Panels (g) and (h) same as panels (a) and (b) except for NOAA20-VIIRS. In comparing the CSZA-only (left column) and with atmospheric correction (right column) plots, note the improved RSB consistency attained by correcting for the atmosphere.
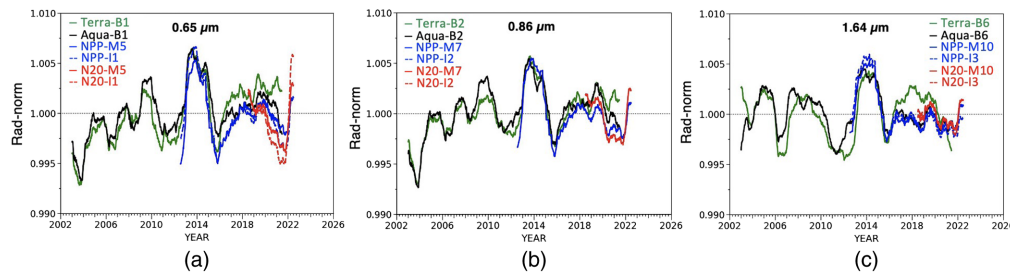
Fig. 11 Libya-4 365-day averaged atmospheric corrected rad$_{norm}$ observations for the (a) 0.65-μm wavelength color coded by satellite and RSB as denoted in the legend. Panel (b) same as panel (a) except for the 0.86-μm bands. Panel (c) same as panel (a) except for the 1.64-μm bands. The MODIS and VIIRS bands are listed in Table 1.

Here, we verify if the atmospheric-corrected rad$_{norm}$ fluctuations are comparable across the MODIS and VIIRS imagers. The 0.65 and 0.86-μm MODIS and VIIRS band rad$_{norm}$ observations are presented in Figs. 11(a) and 11(b), respectively, which show that, indeed, the rad$_{norm}$ temporal fluctuations are in harmony. However, the 1.64-μm band rad$_{norm}$ temporal fluctuations [Fig. 11(c)] differ slightly from their visible counterparts before 2012. The 2014 rad$_{norm}$ inflection is present across all RSB and all sensors, except NOAA20-VIIRS because it was launched in late 2017, suggesting that the atmospheric correction and BRDF inadequacies do not explain the 2014 inflection.

The fact that rad$_{norm}$ inflections are in-synch among the MODIS and VIIRS RSB indicates that the inflections accurately describe the Libya-4 site natural variability and that the sensor calibration anomalies are much smaller than the true Libya-4 natural variability. The inflections being similar between RSBs suggests that the Libya-4 natural variability is mainly owed to prevailing winds changing the orientation of sand dunes that define the areal extent of the shadowing.[24] This finding suggests that (1) the Libya-4 sand color is not changing in time from dust advection, (2) wet sand evaporates quickly from rain events, and (3) the sand dunes prevent any vegetation from growing.

3.3 Libya-4 Temporal Stability

We now quantify the Libya-4 stability by the imager, RSB, and atmospheric correction. Table 4 quantifies the MODIS and VIIRS channel-specific trend$_{SE}$ without (first row of Table 2) and with (second row of Table 2) atmospheric corrections, with the percent trend$_{SE}$ reduction due to atmospheric correction being given in the third row in red text. The NPP and NOAA20 VIIRS M8 and M11 had a ~40% and ~62% trend$_{SE}$ reduction by including the PW term. The Terra and Aqua MODIS B2, B17, B5, and B7 trend$_{SE}$ was reduced by ~35%, 80%, 30%, and 67% with PW correction, respectively. The 1.61-μm wavelength, which is least impacted by the atmosphere, has the smallest RSB trend$_{SE}$, which are within 0.6% and probably represents the Libya-4 natural variability. Most of the water vapor absorbing channel (>0.8 μm) trend$_{SE}$ after atmospheric correction are within 0.7%, indicating that PW mostly accounts for the daily TOA radiance variability. The trend$_{SE}$ atmospheric correction reduction was less than 20% for wavelengths less than 0.6 μm, which implies that a more effective AOD and ozone source or a better pristine clear-sky filtering approach is needed, which is left for future studies. The larger Terra-MODIS 0.48-μm channel trend$_{SE}$, when compared with Aqua-MODIS, are due to unresolved polarization issues.[59] The similarity between MODIS and VIIRS trend$_{SE}$ suggests that the MODIS L1b C6.1 to C7 temporal radiometric adjustments are effective.[61] In general, the Libya-4 trend$_{SE}$ is between 0.6% and 0.75% for wavelengths greater than 0.6 μm and between 0.75% and 1.0% for wavelengths less than 0.6 μm.

We now perform the Libya-4 stability assessment for viewing angles less than 35 deg. It was noted in Sec. 3.1 and Fig. 9(b) that the NPP-VIIRS near-nadir angles have smaller trend$_{SE}$. Similar scan angle dependent trend$_{SE}$ was obtained for MODIS and NOAA20-VIIRS (not shown). Near nadir observations avoid oblique path lengths that require larger atmospheric corrections and three-dimensional sand dune effects. Limiting the viewing angle to 35 deg or less reduces the sampling by ~66%, which decreases the number of clear-sky observations over the

Table 4 Libya-4 Terra-MODIS, Aqua-MODIS, NPP-VIIRS, and NOAA20-VIIRS trend$_{SE}$ by RSB. For each sensor, the first row is based on the CSZA trend$_{SE}$, the second row is the trend$_{SE}$ with atmospheric corrections, and the third row (bold text) is the atmospheric correction trend$_{SE}$ reduction in %.

SAT/BANDS	Libya-4, VZA < 70 deg	0.46 (B3)	0.55 (B4)		0.64 (B1)	0.87 (B2)	0.91 (B17)	1.24 (B5)	1.629 (B6)		2.10 (B7)
Aqua	Cos(SZA)	1.172	0.935		0.868	0.941	5.835	0.846	0.608	—	2.011
	Cos(SZA) + WV + O3 + AOD	0.967	0.837		0.737	0.663	1.192	0.616	0.574	—	0.662
	↓ Δ (%)	**17**	**10**		**15**	**30**	**80**	**27**	**6**	**—**	**67**
Terra	Cos(SZA)	1.639	0.969		0.942	1.053	5.732	0.935	0.660	—	2.189
	Cos(SZA) + WV + O3 + AOD	1.351	0.859		0.719	0.627	1.220	0.627	0.565	—	0.714
	↓ Δ (%)	**18**	**11**		**23**	**40**	**79**	**33**	**14**	**—**	**67**
SAT/BANDS		0.49 (M3)	0.55 (M4)	0.64 (I1)	0.67 (M5)	0.87 (M7)	—	1.24 (M8)	1.629 (M10)	1.61 (I3)	2.20 (M11)
N20	Cos(SZA)	1.101	0.939	0.884	0.725	0.713	—	1.072	0.665	0.673	1.983
	Cos(SZA) + WV + O3 + AOD	1.013	0.838	0.765	0.659	0.629	—	0.643	0.602	0.605	0.758
	↓ Δ (%)	**8**	**11**	**13**	**9**	**12**	**—**	**40**	**9**	**10**	**62**
NPP	Cos(SZA)	1.100	0.885	0.801	0.686	0.748	—	1.051	0.636	0.636	1.923
	Cos(SZA) + WV + O3 + AOD	0.986	0.808	0.696	0.652	0.618	—	0.615	0.560	0.581	0.714
	↓ Δ (%)	**10**	**9**	**13**	**5**	**17**	**—**	**41**	**12**	**9**	**63**

16-day repeat cycle, but it is countered by the increased temporal stability of the near nadir observations. Also, the long-term MODIS Libya-4 reflectance trending by scan angle is much noisier for oblique viewing angles (see Fig. 13, Xiong et al.[59]). The VIIRS instrument was designed to mitigate the response versus scan angle variations by utilizing a rotating telescope assembly and a half angle mirror, unlike MODIS, which relies on a scan mirror.[47]

Table 5 shows the Libya-4 trend$_{SE}$ for viewing angles less than 35 deg and can be directly compared with Table 4, which includes all angles. The RSB dependent atmospheric correction trend$_{SE}$ percentage reductions are similar for near-nadir and full scan conditions. This result suggests that performing atmospheric corrections is effective not just for oblique angle observations but also for nadir observations. A 5% to 23% trend$_{SE}$ reduction was observed by limiting the VZA to 35 deg, depending on the channel. The VIIRS non-absorbing 1.61-μm channel trend$_{SE}$ for VZA less than 35 deg is within 0.50%, whereas for all viewing angles, it was within 0.60%, indicating that the surface reflectance variability is slightly larger for oblique views. Overall, the Libya-4 trend$_{SE}$ for VZA less than 35 deg was between 0.5% and 0.8%, except for the Terra-MODIS B3 channel.

4 Conclusion

This study documents the improved Libya-4 characterization performed by the CERES IGCG, designed to assess the MODIS and VIIRS RSB stability and radiometric scaling between imagers for consistent flux and cloud retrievals. The Libya-4 observations were stratified by orbit repeat day, with the observed angles uniquely corresponding to the repeat day. Pristine clear-sky observations were identified by both broad and angular-bin-specific dynamic spatial homogeneity thresholds, applied to the mostly non-absorptive 0.65 and 1.61-μm channels. The use of spatial

Table 5 Same as Table 4 except for angular bins with VZA < 35 deg.

SAT/BANDS	Libya-4, VZA < 35°	0.46 (B3)	0.55 (B4)		0.64 (B1)	0.87 (B2)	0.91 (B17)	1.24 (B5)	1.629 (B6)		2.10 (B7)
Aqua	Cos(SZA)	0.896	0.834	—	0.803	0.845	5.476	0.743	0.561	—	1.767
	Cos(SZA) + WV + O3 + AOD	0.795	0.755	—	0.655	0.582	1.133	0.552	0.541	—	0.616
	↓ Δ (%)	**11**	**9**	—	**18**	**31**	**79**	**26**	**4**	—	**65**
Terra	Cos(SZA)	1.022	0.845	—	0.817	0.887	5.294	0.782	0.580	—	1.909
	Cos(SZA) + WV + O3 + AOD	0.882	0.770	—	0.656	0.559	1.119	0.563	0.538	—	0.679
	↓ Δ (%)	**14**	**9**	—	**20**	**37**	**79**	**28**	**7**	—	**64**
SAT/BANDS	—	0.49 (M3)	0.55 (M4)	0.64 (I1)	0.67 (M5)	0.87 (M7)	—	1.24 (M8)	1.629 (M10)	1.61 (I3)	2.20 (M11)
N20	Cos(SZA)	0.894	0.838	0.795	0.624	0.579	—	0.850	0.525	0.549	1.554
	Cos(SZA) + WV + O3 + AOD	0.827	0.767	0.698	0.573	0.516	—	0.493	0.484	0.505	0.640
	↓ Δ (%)	**7**	**8**	**12**	**8**	**11**	—	**42**	**8**	**8**	**59**
NPP	Cos(SZA)	0.894	0.783	0.701	0.585	0.645	—	0.892	0.528	0.525	1.550
	Cos(SZA) + WV + O3 + AOD	0.804	0.712	0.596	0.549	0.518	—	0.503	0.487	0.487	0.628
	↓ Δ (%)	**10**	**9**	**15**	**6**	**20**	—	**44**	**8**	**7**	**59**

homogeneity thresholds was effective across all RSBs, thereby eliminating clear-sky reflectance thresholds. For visible bands, the clouds are brighter than the surface, and for SWIR bands, the clouds are darker than the surface reflectance. The clear-sky TOA radiances can be predicted using a second order CSZA relationship derived for each angular bin. The RSB atmospheric radiance contribution was mitigated by including linear PW, O3, and AOD atmospheric correction terms. Several PW, O3, and AOD sources were correlated with the daily clear-sky TOA radiance observations to find the most effective source. The PW correction was most effective, whereas the AOD and O3 corrections were less successful.

The BRDF and atmospheric corrected normalized radiances were validated across angular bins, RSB, and MODIS and VIIRS imagers. The normalized radiances were found to have in-synch angular bin temporal trending, indicating that the atmospheric correction adequately accounted for the various angular bin atmospheric column path lengths, especially for water vapor absorption. The lowest angular bin trend$_{SE}$ values were found at near-nadir conditions, whereas the largest were found for oblique backscatter conditions. The lowest RSB trend$_{SE}$ were found for the M5 and M10 bands, which are least impacted by the atmospheric column, and the highest RSB trend$_{SE}$ were found for the M3 and M4 bands. The normalized radiance temporal fluctuations were similar across the MODIS and VIIRS imagers, except for Terra-MODIS, which experienced onboard calibration system anomalies. This result suggests that the normalized radiance variability describes the true Libya-4 surface reflectance natural variability and that the imager calibration anomalies are much smaller than the natural variability. The Libya-4 surface reflectance natural variability is not dependent on wavelength, but rather is likely owed to the shadowing from the sand dunes, which are shifting in time due to the prevailing winds. The overall imager RSB trend$_{SE}$ was between 0.6% and 1.0%, whereas for scan angles less than 35 deg, the trend$_{SE}$ was 0.5% to 0.8%, with RSB of less than 0.6-μm having the greater trend$_{SE}$.

The Libya-4 full scan characterization permits continuous clear-sky daily monitoring, which is not possible with nadir-only sampling. With all sensors in the same 16-day repeat cycle orbit, it is possible to tie the response versus scan angle across overlapping sensors as the PICS is

characterized by the repeat day. The Aqua-MODIS specific atmospheric correction parameters will need to be updated in the future due to Aqua's decommissioning in late 2026. The MODIS PW-RSB retrieval relies on the 0.9 μm NIR channels. The VIIRS imager does not contain similar NIR channels. The recently launched Meteosat Third Generation (MTG), geostationary satellite flexible combined imager includes a 0.914 μm NIR channel and has the potential to estimate the PW over Libya-4. Otherwise, PW data from GMAO are available. Additionally, the ozone and AOD atmospheric correction strategy will be reexamined, with the possibility of adding a Rayleigh scattering term.

The Libya-4 full scan and atmospheric RSB characterization reveals that the short-term surface reflectance anomalies in PICS must be considered when assessing imager stability and performing sensor inter-calibration. This level of PICS characterization was only possible using the well calibrated MODIS and VIIRS radiances as well as using reliable PW, ozone, and AOD daily observations. This study does not address long-term Libya-4 surface reflectance stability beyond the MODIS and VIIRS records or for imagers located in other mean local time Sun-synchronous orbits. It is possible that the long-term surface reflectance variation can be correlated to the prevailing winds. For overlapping sensor records in the same orbit, all concurrent sensors should observe the same Libya-4 surface reflectance anomalies. A sensor deviating from the family of concurrent imagers would indicate a sensor calibration anomaly. To inter-calibrate sensor pairs in the same orbit, the PICS reflectance anomaly can be mitigated by taking the ratio of the sensor pair's monthly normalized radiances. The CERES IGCG is currently analyzing the time series of CERES broadband SW radiances over Libya-4. Preliminary results indicate that the overall broadband response natural variability over Libya-4 is relatively smaller compared with the natural variability observed in the multispectral bands of MODIS and VIIRS. We are working on a quantitative characterization of the CERES broadband SW radiances and associated natural variability over Libya-4, leveraging this information for monitoring and intercalibrating CERES SW radiometers across different platforms. These findings will be detailed in a forthcoming article.

Disclosures

No conflicts of interest, financial or otherwise, are declared by the authors.

Code and Data Availability

The NASA MODIS C6.1 L1b and the NASA VIIRS Land Science Investigator-led Processing System (Land SIPS) L1b Collection 2 products are available at the LAADS DAAC (https://ladsweb.modaps.eosdis.nasa.gov/#level0-level1). The MODIS C6.1 radiances were converted to C7 using LUTs provided by the MODIS Characterization Support Team (MCST). The MOD08 and MYD08 product are available at the LAADS DAAC (https://ladsweb.modaps.eosdis.nasa.gov/missions-and-measurements/products/MYD08_D3). The NASA CERES SYN1deg and SSF1deg products are available at the CERES visualization and ordering tool (https://ceres.larc.nasa.gov/data/). The spatial averaging algorithms and linear regression routines are community standard methods and the coding framework is documented in Fig. 1.

Acknowledgments

References

1. B. A. Wielicki et al., "Clouds and the Earth's Radiant Energy System (CERES): an Earth observing system experiment," *Bull. Am. Meteorol. Soc.* **77**(5), 853–868 (1996).
2. N. G. Loeb et al., "Clouds and the Earth's Radiant Energy System (CERES) Energy Balanced and Filled (EBAF) top-of-atmosphere (TOA) edition-4.0 data product," *J. Clim.* **31**(2), 895–918 (2018).
3. W. Su et al., "Next-generation angular distribution models for top-of-atmosphere radiative flux calculation from CERES instruments: validation," *Atmos. Meas. Tech.* **8**, 611–632 (2015).
4. Q. Z. Trepte et al., "Global cloud detection for CERES Edition 4 using terra and aqua MODIS data," *IEEE Trans. Geosci. Remote Sens.* **57**(11), 9410–9449 (2019).

5. P. Minnis et al., "CERES MODIS cloud product retrievals for edition 4, Part I: algorithm changes," *IEEE Trans. Geosci. Remote Sens.* **59**(4), 2744–2780 (2021).

6. C. R. Yost et al., "CERES MODIS cloud product retrievals for edition 4—Part II: comparisons to CloudSat and CALIPSO," *IEEE Trans. Geosci. Remote Sens.* **59**(5), 3695–3724 (2021).

7. D. R. Doelling et al., "Geostationary enhanced temporal interpolation for CERES flux products," *J. Atmos. Ocean. Technol.* **30**(6), 1072–1090 (2013)

8. R. Bhatt et al., "Clouds and the Earth's Radiant Energy System strategy for intercalibrating the new-generation geostationary visible imagers," *J. Appl. Rem. Sens.* **14**(3), 032410 (2020).

9. https://www.nesdis.noaa.gov/our-satellites/currently-flying/joint-polar-satellite-system.

10. J. Sun et al., "Time-dependent response versus scan angle for MODIS reflective solar bands," *IEEE Trans. Geosci. Remote Sens.* **52**(6), 3159–3174 (2014).

11. R. Bhatt et al., "Characterizing response versus scan-angle for MODIS reflective solar bands using deep convective clouds," *J. Appl. Rem. Sens.* **11**(1), 016014 (2017).

12. EROS Cal/Val Center of Excellence (ECCOE) Test Sites Catalog: Libya-4, 2021, https://calval.cr.usgs.gov/apps/libya-4 (accessed 6 August 2024).

13. W. F. Staylor, "Site selection and directional models of deserts used for ERBE validation targets," NASA-TP 2540, 12 (1986).

14. W. F. Staylor, "Degradation rates of the AVHRR visible channel for the NOAA 6, 7, and 9 spacecraft," *J. Atmos. Ocean. Technol.* **7**(3), 411–423 (1990).

15. C. R. Nagaraja Rao, M. P. Weinreb, and J. Chen, "Recalibration of the advanced very high resolution radiometer for climate change research," *Adv. Space Res.* **14**(1), 117–120 (1994).

16. H. Cosnefroy, M. Leroy, and X. Briottet, "Selection and characterization of Saharan and Arabian desert sites for the calibration of optical satellite sensors," *Remote Sens. Environ.* **58**(1), 101–114 (1996).

17. P. M. Teillet et al., "Prime candidate Earth targets for the post-launch radiometric calibration of satellite sensors," *Proc. SPIE* **6677**, 66770S (2007).

18. D. L. Helder, B. Basnet, and D. L. Morstad, "Optimized identification of worldwide radiometric pseudo-invariant calibration sites," *Can. J. Remote Sens.* **36**(5), 527–539 (2010).

19. C. Bacour et al., "Revisiting Pseudo Invariant Calibration Sites (PICS) over sand deserts for vicarious calibration of optical imagers at 20 km and 100 km scales," *Remote Sens.* **11**, 1166 (2019).

20. A. K. Heidinger et al., "Deriving an inter-sensor consistent calibration for the AVHRR solar reflectance data record," *Int. J. Remote Sens.* **31**(24), 6493–6517 (2010).

21. R. Bhatt et al., "A consistent AVHRR visible calibration record based onmultiple methods applicable for the NOAA degrading orbits. Part I: Methodology," *J. Atmos. Ocean. Technol.* **33**, 2499–2515 (2016).

22. D. R. Doelling et al., "A consistent AVHRR visible calibration record based on multiple methods applicable for the NOAA degrading orbits. Part II: Validation," *J. Atmos. Ocean. Technol.* **33**, 2517–2534 (2016).

23. C. Li et al., "Post calibration of channels 1 and 2 of long-term AVHRR data record based on SeaWiFS data and pseudo invariant targets," *Remote Sens. Environ.* **150**, 104–119 (2014).

24. Y. M. Govaerts, "Sand dune ridge alignment effects on surface BRF over the Libya-4 CEOS calibration site," *Sensors* **15**(2), 3453–3470 (2015).

25. A. Wu et al., "Monitoring MODIS calibration stability of visible and near-IR bands from observed top-of atmosphere BRDF-normalized reflectances over Libyan Desert and Antarctic surfaces," *Proc. SPIE* **7081**, 708113 (2008).

26. R. Bhatt et al., "Desert-based absolute calibration of successive geostationary visible sensors using a daily exoatmospheric radiance model," *IEEE Trans. Geosci. Remote Sens.* **52**, 3670–3682 (2014).

27. D. Doelling et al., "Geostationary visible imager calibration for the CERES SYN1deg edition 4 product," *Remote Sens.* **10**, 288 (2018).

28. T. Chang et al., "Aqua and terra MODIS RSB calibration comparison using BRDF modeled reflectance," *IEEE Trans. Geosci. Remote Sens.* **55**(4), 2288–2298 (2017).

29. N. Mishra et al., "Absolute calibration of optical satellite sensors using Libya 4 pseudo invariant calibration site," *Remote Sens.* **6**, 1327–1346 (2014).

30. A. Wu and Q. Zhong, "A method for determining the sensor degradation rates of NOAA AVHRR channels 1 and 2," *J. Appl. Meteorol. (1988-2005)* **33**(1), 118–122 (1994).

31. A. Wu et al., "Characterization of terra and aqua MODIS VIS, NIR, and SWIR spectral bands' calibration stability," *IEEE Trans. Geosci. Remote Sens.* **51**(7), 4330–4338 (2013).

32. R. Bhatt et al., "An initial assessment of the VIIRS onboard calibration using DCC and desert referenced to the Aqua-MODIS calibration," *Proc. SPIE* **8866**, 88660K (2013).

33. R. Bhatt et al., "Initial stability assessment of S-NPP VIIRS reflective solar band calibration using invariant desert and deep convective cloud targets," *Remote Sens.* **6**, 2809–2826 (2014).

34. D. R. Doelling et al., "The radiometric stability and scaling of collection 6 Terra and Aqua-MODIS VIS, NIR, and SWIR spectral bands," *IEEE Trans. Geosci. Remote Sens.* **53**(8), 4520–4535 (2015).

35. D. R. Doelling et al., "Additional characterization of Libya-4 in support of post-launch vicarious calibration of satellite imagers," *Proc. SPIE* **12232**, 1223219 (2022).

36. D. R. Doelling et al., "Improved characterization of Libya-4 and Dome-C for consistent radiometric scaling between VIIRS sensors," *Proc. SPIE* **12685**, 1268519 (2023).

37. F. Yu and X. Wu, "Water vapor correction to improve the operational calibration for NOAA AVHRR/3 channel 2 (0.85-μm) over a desert target," *Can. J. Remote Sens.* **36**(5), 514–526 (2010).

38. D. Helder et al., "Absolute radiometric calibration of Landsat using a pseudo invariant calibration site," *IEEE Trans. Geosci. Remote Sens.* **51**, 1360–1369 (2013).

39. C. S. R. Neigh et al., "Monitoring orbital precession of EO-1 hyperion with three atmospheric correction models in the Libya-4 PICS," *IEEE Geosci. Remote Sens. Lett.* **13**(12), 1797–1801 (2016).

40. B. Raut et al., "Empirical absolute calibration model for multiple pseudo-invariant calibration sites," *Remote Sens.* **11**, 1105 (2019).

41. M. D. Chaity et al., "Hyperspectral empirical absolute calibration model using Libya 4 pseudo invariant calibration site," *Remote Sens.* **13**, 1538 (2021).

42. M. Bouvet, "Radiometric comparison of multispectral imagers over a pseudo-invariant calibration site using a reference radiometric model," *Remote Sens. Environ.* **140**, 141–154 (2014).

43. A. Lyapustin et al., "Scientific impact of MODIS C5 calibration degradation and C6+ improvements," *Atmos. Meas. Tech.* **7**, 4353–4365 (2014).

44. S. Lee, G. Meister, and B. Franz, "MODIS aqua reflective solar band calibration for NASA's R2018 ocean color products," *Remote Sens.* **11**, 2187 (2019).

45. A. Angal et al., "Assessing the calibration differences in the reflective solar bands of Terra MODIS and Landsat-7 enhanced thematic mapper plus," *J. Appl. Remote Sens.* **12**(4), 044002 (2018)

46. X. Fan and Y. Liu, "Quantifying the relationship between intersensor images in solar reflective bands: implications for intercalibration," *IEEE Trans. Geosci. Remote Sens.* **52**(12), 7727–7737 (2014).

47. K. Twedt et al., "MODIS reflective solar bands calibration improvements for Collection 7," *Proc. SPIE* **11858**, 118580S (2021).

48. M. M. Rienecker et al., "GMAO: NASA's modern-era retrospective analysis for research and applications," *J. Clim.* **24**, 3624–3648 (2011).

49. Y. J. Kaufman and B. -C. Gao, "Remote sensing of water vapor in the near IR from EOS/MODIS," *IEEE Trans. Geosci. Remote Sens.* **30**(5), 871–884 (1992).

50. J. He and Z. Liu, "Comparison of satellite-derived precipitable water vapor through near-infrared remote sensing channels," *IEEE Trans. Geosci. Remote Sens.* **57**(12), 10252–10262 (2019).

51. S. W. Seemann et al., "Operational retrieval of atmospheric temperature, moisture, and ozone from MODIS infrared radiances," *J. Appl. Meteorol. Climatol.* **42**, 1072–1091 (2003).

52. R. C. Levy et al., "Global evaluation of the Collection 5 MODIS dark-target aerosol products over land," *Atmos. Chem. Phys.* **10**, 10399–10420 (2010).

53. N. C. Hsu et al., "Enhanced deep blue aerosol retrieval algorithm: the second generation," *J. Geophys. Res. Atmos.* **118**, 9296–9315 (2013).

54. W. D. Collins et al., "Simulating aerosols using a chemical transport model with assimilation of satellite aerosol retrievals: methodology for INDOEX," *J. Geophys. Res.* **106**(D7), 7313–7336 (2001).

55. CERES_SYN1deg_Ed4A Data Quality Summary, 2021, https://ceres.larc.nasa.gov/documents/DQ_summaries/CERES_SYN1deg_Ed4A_DQS.pdf (Accessed 6 August 2024).

56. MYD08_D3 - MODIS/Aqua Aerosol Cloud Water Vapor Ozone Daily L3 Global 1Deg CMG, https://ladsweb.modaps.eosdis.nasa.gov/missions-and-measurements/products/MYD08_D3 (Accessed 6 August 2024).

57. S. Uprety and C. Cao, "Suomi NPP VIIRS reflective solar band on-orbit radiometric stability and accuracy assessment using desert and Antarctica Dome C sites," *Remote Sens. Environ.* **166**, 106–115 (2015).

58. J. L. Roujean, M. Leroy, and P. Y. Deschamp, "A bidirectional reflectance model of the Earth's surface for the correction of remote sensing data," *J. Geophys, Res.* **97**, 20455–20468 (1992).

59. X. Xiong et al., "MODIS reflective solar bands on-orbit calibration and performance," *IEEE Trans. Geosci. Remote Sens.* **57**(9), 6355–6371 (2019).

60. X. Shao et al., "Surface roughness-induced spectral degradation of multi-spaceborne solar diffusers due to space radiation exposure," *IEEE Trans. Geosci. Remote Sens.* **57**(11), 8658–8671 (2019).

61. X. Xiong et al., "MODIS and VIIRS calibration and characterization in support of producing long-term high-quality data products," *Remote Sens.* **12**, 3167 (2020).

David R. Doelling leads the NASA Clouds and the Earth's Radiant Energy System (CERES) Time Interpolated and Spatially Averaged Working Group and is responsible for temporally averaging the CERES fluxes and clouds into level-3 products. He incorporates hourly geostationary (GEO) derived broadband fluxes to infer the regional diurnal cycle, requiring his focus on GEO

imager calibration. He is the Global Space-based Inter-Calibration System visible calibration lead.

Conor Haney received his BS and MS degrees in atmospheric sciences from the University of Illinois at Urbana–Champaign, Champaign, Illinois, United States, in 2010 and 2013, respectively. He is currently a research scientist at the Analytical Mechanics Associates, Hampton, Virginia, United States, supporting NASA Langley Research Center contracts. He is responsible for maintaining the real-time visible sensor calibration of geostationary satellite imagers for the NASA CERES project.

Prathana Khakurel is a research scientist at Analytical Mechanics Associates in Hampton, Virginia, United States. She supports the CERES project at NASA Langley Research Center by developing in-flight calibration techniques for geostationary and low-Earth orbiting satellite sensors. She received her master's degree in electrical engineering, specializing in remote sensing, from South Dakota State University in South Dakota, United States, in 2021.

Rajendra Bhatt is currently supporting the CLARREO Pathfinder (CPF) project at NASA Langley Research Center as the deputy project scientist for intercalibration studies. Prior to joining CPF, he worked on the CERES project for 12 years developing techniques for in-flight calibration of geostationary and low Earth-orbiting satellite imagers to assess their radiometric performance on orbit and ensure the usability of the satellite observations for climate studies.

Benjamin Scarino is employed by NASA as a senior research scientist supporting the Climate Science Branch of the NASA Langley Research Center Science Directorate. As part of his work for the NASA CERES program, he supports the development of global multispectral cloud and surface property retrieval algorithms as well as satellite calibration/validation efforts. He is a specialist on intercalibration techniques and determining corrections for instrument spectral band differences.

Arun Gopalan received his BS degree in mechanical engineering from the University of Bombay, Mumbai, India, in 1991 and his MS degree in mechanical engineering from the State University of New York, Stony Brook, New York, United States, in 1993. He is currently a senior research scientist at the Analytical Mechanics Associates, Hampton, Virginia, United States, in support of the NASA Langley Research Center's CERES and Climate Absolute Radiance and Refractivity Observatory projects.